4.4
Heat Transfer Analysis

Frank J. Cunha, Ph.D., P.E.

Pratt & Whitney
United Technologies Corporation
5 Bruce Lane
Avon, CT 06001

Phone: (860) 565-8909
Email: frank.cunha@pw.utc.com

4.4-1 Introduction

The thermal efficiency and specific output of a gas turbine are primarily dependent on two major cycle parameters: the pressure ratio and the turbine inlet temperature[1]. In an ideal Brayton cycle, thermal efficiency increases up to stoichiometric temperatures and high-pressure ratios, without considering losses, particularly, those associated with turbine cooling. Since turbine airfoil materials melt at temperatures much lower than the stoichiometric temperatures, hot gas-path components, such as turbine airfoils, must be cooled and attention must be given to cycle parasitic losses.

The recognition of material temperature limitations has led to the continuous turbine development programs for cooling technologies, material development, and related multi-disciplinary disciplines of fluid dynamics, heat transfer, aerodynamic performance, and structures, all aimed at the durability of turbine hot-gas-path components. The pursuit of improved turbine materials began long ago when the initial temperature limitations were found to be at about 1500°F (800°C)[2]. Following this initial period, an intensive development period took place when nickel-based alloys were developed and characterized as having high creep resistance characteristics. Material improvements relaxed temperature limitations by about 300°F (167°C)[3]. Further development of turbine airfoil manufacturing techniques, such directionally-solidification castings and single-crystal castings led to higher metal temperature capability. More recently, numerous testing evaluations have been conducted to characterize new hot-gas path material superalloys in terms of tensile, rupture, fatigue, creep, toughness, corrosion and oxidation resistances, producibility, processing, and other thermophysical properties[4]. Following extensive laboratory testing, actual operating experience is gained with engine testing subject to real operational environments culminating in mature levels of technology readiness levels for production.

Today, many modern turbine airfoils use single crystal superalloys. These are two-phase alloys with a large volume fraction of γ' precipitates, based on the intermetallic compound, Ni_3Al, interspersed in a coherent face-centered cubic γ matrix comprised of nickel, Ni, with smaller weight percent of various other elements in solid solution[5]. These elements include: cobalt, Co, aluminum, Al, chromium, Cr, tungsten, W, molybdenum, Mo, tantalum, Ta, hafnium, Hf, rhenium, Re, and ruthenium, Ru. The elements Re and Ru are introduced in the latest generation of single crystal alloys. All these elements have different attributes which can be summarized as follows: Cr, Al, and Hf are used as surface protection elements, Mo, W, and Ta are used in solid solution strengthening, and Re and Ru are used for high creep strength[6].

The strength of these single crystal alloys is mainly a function of the size and the percentage of γ' precipitates. Experimentally, it has been determined that the peak creep strength is achieved with a volume fraction of γ' of 60%-65%[7]. Much of the behavior of these alloys can be explained on the basis that high volume fraction γ' alloys deformation occurring by shearing of the γ' precipitates. The high volume fraction of precipitates precludes dislocation bypass at low and intermediate temperatures forcing precipitate shearing. However, the energies resisting dislocation shearing of the precipitates are those required to form a local reversal of Al-Ni order or antiphase boundary in stacking fault of the Ni_3Al superlattice. The energies associated with the anti-phase boundary in the superlattice stacking faults determine the strength, fatigue, and fracture characteristics of these alloys[8]. This is also evident by the increase in yield strength at moderate to high temperatures before a monotonic decrease in yield strength. As a result, the excellent high-temperature creep and fatigue resistance of the superalloys is a result of a combination of solid-solution strengthening, absence of deleterious grain boundaries, and high volume fraction of precipitates that act as barriers to dislocation motion. It should be pointed-out, however, that fatigue crack initiation also depends on the microscopic

defects, which can be categorized as intrinsic defects and deviant material defects. Intrinsic defects include carbides, undissolved eutectic pools, and associated micro-porosity, concentrated in interdendritic regions of the casting. Even though the intrinsic defects are normal features of the alloy microstructure, deviant defects, such as crystallographic defects related to low and high angle grain boundaries, freckles and silver grains, and porosity, are considered rejectable defects in the material quality that exceeds specified limits. Modern single crystal superalloys are face-centered single crystal superalloys with cubic symmetry. As a result, there are three independent mechanical properties that characterize the material behavior: the modulus of elasticity, E, the shear modulus, G, and the Poisson ratio, v[9]. The mechanical and thermal-physical properties are also a function of temperature and change with crystal orientation leading to anisotropic behavior of the material. After the casting process, a series of standard heat treatments, such as, solution annealing, coating heat treatment, and precipitation heat treatment, are used to optimize microstructures of the material[10].

In parallel to base material development, coatings were also developed to protect the base material from corrosion and oxidation attack[11]. These coatings were designated as metallic bond coatings characterized as diffusion and overlay type coatings. The substantive difference between the overlay and diffusion type coatings relies on the how the coating constituents are supplied. For diffusion type coatings, the major constituents are supplied by the base metal; whereas, for overlay coatings, the constituents are supplied by external coating sources. The advantage of overlay coatings is that more varied corrosion and oxidation resistant compositions can be applied with increased bonding thickness. The surface roughness of bond coatings allow for the deposition of ceramic type thermal barrier coatings. The addition of these coating systems onto single crystal superalloy substrate has further relaxed the temperature limitations associated with the turbine inlet conditions. As the material development of coatings and base material reach a culminating point, further increases in turbine inlet temperatures can only come from advanced airfoil cooling. Thus, cooling and material technologies have permitted designs with turbine inlet conditions in excess of 3100°F (1700°C) with interface bond-to-metal temperatures topping at 2050°F (1121°C) for durability requirements of oxidation, creep life, and fatigue cycles[12].

Two of the most relevant parameters for measuring and assessing cooling performance of turbine airfoils are the cooling effectiveness parameter and heat load parameter. By definition, this parameter is a dimensionless temperature ratio of gas-to-metal temperature difference over the gas-to-coolant temperature difference[13]:

$$\varphi = \frac{T_{gas} - T_{metal}}{T_{gas} - T_{c,in}} \quad . \tag{1}$$

Clearly, if the cooling effectiveness is non-existent, or zero, there is no cooling effect; whereas, if the cooling effectiveness is equal to unity, the airfoil metal and coolant temperature are the same. These two extreme values of either zero or unity are considered as outer limits for cooling effectiveness parameter. In general, the cooling effectiveness lies in-between these two limits and characterizes the performance of the cooling circuit inside the turbine airfoil.

The other parameter denoted as the heat load parameter is defined as the ratio of internal heat to the external heat fluxes as follows[14]:

$$\beta = \frac{(m\ c_p)_{coolant}}{(h\ A)_{gas}} \quad . \tag{2}$$

Figure 1 illustrates cooling effectiveness for typical cooling configurations as a function of heat load parameter simplified here just by the variable in cooling flow[15]. The cooling effectiveness is naturally a function of many design variables, that is, the cooling configuration, and the coolant ejection requirements. It also a strong function of the amount of cooling medium used, usually measured as percentage of the mainstream gas. As illustrated in figure 1, the cooling effectiveness increases rapidly with small amounts of coolant. Then, the cooling effectiveness increases monotonically at a lower rate. This implies that for demanding thermal applications, where the thermal load parameter is high, large amounts of coolant may be required. For state-of-the-art engines, turbine cooling air and leakage may be as high as 25-30% of engine mainstream flow. In terms of efficiency, and since the cooling air is drawn from the compressor, which is driven by the turbine, it represents a direct loss of efficiency. In general, a very approximate rule-of-thumb of 1% cooling air may represent a loss of a fraction of that percentage in specific fuel consumption. This leads to the obvious conclusion that turbine cooling needs to be minimized. Clearly, this is not the only loss mechanism in the engine. Other losses may include mixing and aerodynamic losses, such as profile drag, skin-friction, gas diffusion, secondary flows, tip clearance, boundary-layer separation, shocks, losses due to off-design airfoil incidence angles, trailing edge vortex shedding, and blockage losses[16]. All these losses of engine cycle and turbine efficiencies have to be set against the gains in running the engine at higher turbine inlet temperatures for maintaining required output. Therefore, it is always necessary to reduce and optimize the cooling air requirements for a gas turbine engine design.

In figure 1, the simplest cooling configuration is characterized by the lowest cooling effectiveness. For instance, the radial cooling holes in the middle of the airfoil cross-section will not permit air to eject from the airfoil walls into the gas mainstream, avoiding film cooling and corresponding ejection mixing losses. However, forced convection through the radial holes may not be sufficient for high

thermal load applications, and even at low thermal loads, this simple cooling arrangement is likely to induce high temperature gradients between the airfoil surface and the cooling hole locations. An improved cooling arrangement over the radial cooling hole arrangement is the multi-pass serpentine cooling configuration. In serpentine cooling arrangements, coolant enters the airfoil through the blade root inlet; passes though multiple circuits, cooling the mid-body of the airfoil before ejecting out of the airfoil through main body film holes or trailing edge slots. The leading edge, with high thermal loads, may be cooled with dedicated cooling circuits. If the leading edge and the mid-body circuits are combined and coupled together, one can refer to these arrangements as cold-bridge or warm-bridge designs depending on the feed source. If the feed coolant comes from the mid-body with freshly supplied coolant, we have a cold-bridge cooling design; whereas, if the feed comes from the mid-body with warmed coolant, naturally after heat pick-up from the mid-body serpentine arrangement, we have a warm-bridge cooling design. Since the serpentine cooling circuits have large wet perimeters in the turbine airfoil cross-section, it is possible to introduce trips on the airfoil internal wall to promote turbulence and enhance internal coolant heat pick-up. Many trip configurations have been designed throughout the years of cooling technology development. These include normal trips, skewed trips, and angled "chevron" trips with different orientations relative to the flow, different trip heights, different height-to-pitch ratios, different relative positioning with respect to each other, either in a staggered or in-line arrangements. These different arrangements lead to different heat transfer characteristics enhancing heat pick-up by the coolant flowing in the serpentine passages tailored to minimize the effects of local external heat loads.

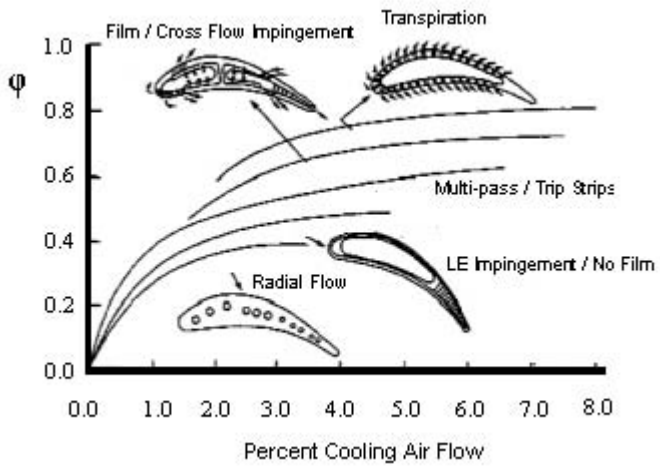

Fig. 1. Cooling effectiveness illustration for different modes of cooling

Source: See note 1.

Further cooling improvements are obtained by the introduction of peripherally cooled airfoil designs. This is done to maintain the greatest thermal gradient within a thin outer layer of the airfoil wall. In addition, the coolant can be ejected at many points around the surface of the airfoil. This concept leads to an increase of convective cooling efficiency by means of peripheral cooling circuits. This new parameter can also be regarded as a dimensionless temperature ratio of the difference between the exit coolant to inlet coolant temperatures relative to the difference of metal to coolant inlet temperatures[17]:

$$\eta_c = \frac{T_{c,out} - T_{c,in}}{T_{metal} - T_{c,in}} \quad . \tag{3}$$

If this ratio is non-existent, or zero, it is implied that exit coolant temperature and inlet temperature are the same, and thus, no heat pick-up in the circuit. If the ratio is unity, then the exit coolant temperature and the metal temperature are the same. In this case, it is said that the cooling circuit is 100% efficient convectively. In general, serpentine cooling may be in the order of 15-30% efficient. However, dedicated airfoil peripheral cooling may be 30-60% efficient. This is about 2X the convective efficiency values of typical serpentine cooling. In addition to the improved convective characteristics, film cooling can be used in many points of the airfoil. The film effectiveness is also a dimensionless parameter defined as [18]:

$$\eta_f = \frac{T_{gas} - T_{film}}{T_{gas} - T_{c,out}} \quad . \tag{4}$$

The overall cooling effectiveness, being a function of both the convective and film cooling effectiveness, can be optimized for any cooling arrangement. If the film exit shape is optimized to cover the airfoil as much as practical, one can obtain overall cooling effectiveness in excess of 75% with film coverage and convective efficiency in excess of 50%. Simply stated, the peripheral airfoil circuits will pick-up heat by convection in a very effective manner and then eject from film openings with high coverage designs to further reduce the thermal load to the part.

It should be noted that the thermal load can be reduced externally by the effect of thermal barrier coating. This is a ceramic coating that is applied on top of the metallic bond coating. The net result is the ability to increase the inlet turbine temperature to values in excess of 3100°F (1700°C) while maintaining interface bond-to-metal temperatures at 2050°F (1121°C) for desired life requirements of oxidation, creep life, and thermal-mechanical fatigue cycles[19]. In the limit, combination of peripheral convective cooling and film may lead to airfoil transpiration cooling which would occur in micro-porous surface to form a continuous film blanketing of the airfoil surface as illustrated in figure 1.

Regarding the different cooling schemes, peripheral cooling and conventional serpentine cooling arrangements may include several internal design features for augmenting internal heat transfer. These internal features may be small posts connected to both sides of the coolant passage, as pedestals, or may project to only about half of the coolant passage, as pin-fins[20]. Fundamentally, both features act in a similar manner, by turbulating coolant flow field and by exposing more surface area to the coolant. These synergistic cooling effects lead to higher internal heat transfer coefficients, which can be regarded as a measure of heat pick-up by the coolant. It should also be noted that there are conduction paths integrated directly with the walls of the airfoil for further cooling. The disadvantage of such augmentation devices is that they increase the coolant flow blockage, which in turn increases the coolant pressure drop. Since the coolant supply pressure may be limited, attention must be given to these blockage effects so as to assure sufficient pressure at the film openings and overcome external gas pressure. The internal-to-external pressure ratio is usually referred to as the back-flow-margin with minimum values established for the leading edge and mid-body of the airfoil. On the other hand, if the internal coolant pressure is much higher than the external pressure at the film exits, then the film jets may actually penetrate through the external boundary layer setting out "blow-off" conditions. Blowing the coolant out nearly normal to the airfoil surface with high velocity is likely to lift the coolant right off the blade and allow the hot mainstream gas to move below the coolant jets making contact with the airfoil surface. This is an adverse film effect that needs to be prevented. To prevent blow-off conditions, the geometrical attributes of film openings need to reduce the ejection velocity by introducing cooling hole shapes, angles, tapering, or diffusion zones while maintaining a high degree of cooling hole filling[21]. Externally in the main flow field, a mismatch between the gas mainstream and the coolant jet velocities will give rise to mixing losses. In this way, film ejection may trip or further energize the external boundary layer; thus, increasing the external heat transfer coefficient or thermal load to the part.

Figure 2 and 3 illustrates typical airfoil cooling schemes. Typically, for the first vane, the coolant is fed into the casing plenum chamber, and from there into the leading edge impingement baffle. From the leading edge baffle, the coolant impinges on the leading edge target surface and is ejected into the external gas-path through several close-spaced rows of holes known generally as shower-head holes. For this component, the highest temperature occurs at the leading edge where the stagnation point is located[22]. The balance of the coolant flow in this vane will pass through a small gap between the baffle and the internal wall of the airfoil leading to other film holes or slots in the main body or trailing edge. Note that internal cooling is done by convective and impingement cooling. At the trailing edge pedestals may be placed to enhance internal cooling, heat pick-up, and decrease the metal temperature[23]. The first blade shown in figure 3 is only an example of a wide variety of serpentine cooling configurations. Stators and rotor blades of downstream stages will often have multi-pass cooling of the type shown in figure 2. The coolant flow is led through a series of serpentine passages and makes several passes along the span before finally ejecting at the trailing edge.

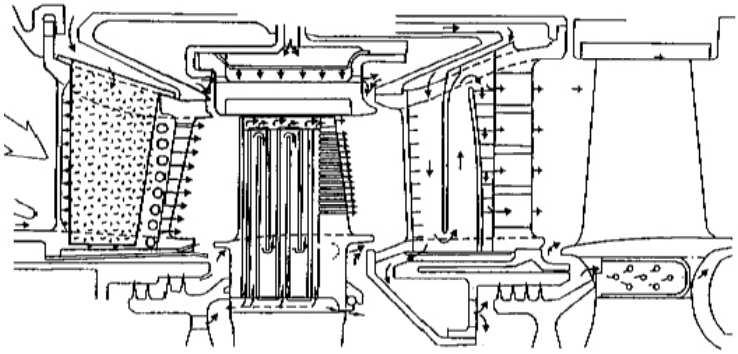

Fig. 2. Typical airfoil cooling schemes for a two-stage high pressure turbine illustrating different modes of cooling.

Source: See Note 1.

The purpose of turbine cooling is solely justified by the need to have turbine components withstand adverse environments while maintaining life targets. Lifing and durability of airfoils require a synthesis of mission cycle, range of operating conditions and time spent at each condition, including the number of transients between conditions. Overall cooling effectiveness is a function of the design, which is reflected by two other relevant parameters: the convective efficiency and the film effectiveness. The overall cooling effectiveness should balance the external heat load to the part. In turn, all cooling parameters need to be balanced with their effects of aerodynamic and cycle performance. For blades, the mechanical load, due to centrifugal effects, need to be determined in conjunction with the blade bulk metal temperature distributions to evaluate its creep capability. The next sections will describe turbine airfoil requirements for the purposes of converting energy to produce shaft power output, or specific core power in a manner where the figure of merit associated with thrust specific fuel consumption is optimized with the thrust-to-weight ratio in the case of aircraft engine applications. In this context, external and internal heat transfer details are explicitly listed and discussed. A section on durability is presented to describe most of the design problems and possible solutions. Conclusions are then derived based on current assessment methods for airfoil cooling technology advancements.

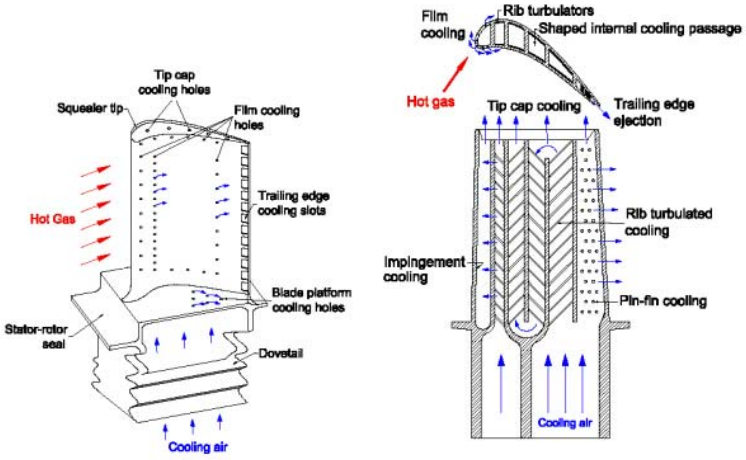

Fig. 3. Typical airfoil cooling schemes for high-pressure turbine blade.

Source: See Note 30.

4.4-2 Heat Transfer Requirements

The primary components of gas turbine engines used in aircraft operations comprise the inlet duct, fan, compressor(s), combustors, turbine(s), and nozzle[24]. Many engines have two turbines: the high and the low-pressure turbine. The high-pressure turbine is required to drive the high-pressure compressor. Together with the combustor, these high-pressure, high-temperature, and high rotating-speed components make up the gas generator portion of the engine. The high-pressure turbine is the most challenging component of the engine design. Most of the attention given in this section covers the turbine limits, and the cooling required to withstand extremely hot, corrosive, and unsteady environments. The low-pressure turbine drives the fan and the low-pressure compressor. The low-pressure turbine is subjected to much cooler gas temperatures. In power applications, another turbine may be added to drive a rotor, a generator, a pump, or a gas compressor. In land-based gas turbine applications, the compressor work is extracted from the first rotor stages, while the other stages produce useful shaft work transformed into electrical power by the electrical generator connected in tandem.

In traditional power generating plants, there are three fundamental elements: (1) the heat source, (2) the heat utilizer, and (3) the waste heat reservoir[25]. To produce useful work heat is supplied by a working fluid from the heat source. The utilizer is required to convert portion of the heat supplied by the working fluid into useful power. Since not all heat can be converted to useful power, a waste reservoir is required to dispose of the remainder of heat. These are the elements of a modern steam plant which can be divided into two major sub-parts: One half consists of the boiler or nuclear reactor as the heat source with its auxiliaries; and the other, the turbine cycle, consisting of turbine generator, condenser, pumps and feed-water heaters. The major components in the turbine cycle are the heat utilizer and the refrigerator or water heat reservoir. In general steam comes from the boiler drum or nuclear reactor, passes through the turbine, which produces mechanical power on the turbine shaft to drive a generator of electrical energy for distribution. Thermodynamic performance is reflected in the overall cycle efficiency, often times designated as the plant heat balance, which is a measure of thermal energy conversion to electrical generation output in BTU per KW-hr.

In land-based power-producing applications, recent improvements in cycle heat balance have being achieved by combining the operations of steam and gas turbines together in the same plant[26]. In these combined cycle plants, the elevated exhaust gas temperature is used in heat recovery steam-generator to create steam before expanding through a train of steam turbines. Intermediate pressure steam is then used as cooling medium in the gas turbine topping cycle. This is done in a closed loop circuit with reheated steam from the gas turbine being returned to the steam turbine cycle for further expansion. In this layout, all gas turbine stationary and rotating airfoils were designed with steam cooling in a closed-loop system. The main reason for this closed cooling system is to avoid losses associated with coolant ejection onto the main gas stream from airfoil locations. Combined power plants operate at thermodynamic cycle efficiencies as high as 60 percent or a heat balance as low as 5700 BTU/KW-hr. One such unit is the GE H-class machine operating at just under 60 percent at Baglan Bay power plant in Wales, UK[27]. This is remarkable, since current advanced nuclear generating plants operate at an overall cycle efficiency of 32.5 percent or at a heat balance of about 10,500 BTU/KW-hr.

4.4-3 Gas Heat Transfer

Regardless of the type of power plant cycle, it is common knowledge that a design of the turbine engine is very challenging, and it requires a mix of technical disciplines: cycle analysis, aerodynamic, heat transfer, combustion, fluid dynamics, and turbine mechanical design and manufacturing. The basic cycle parameters define the engine capability for all operating modes. The overall design is selected in concert with performance and mechanical design constraints. For instance, in gas turbine design, the average heat transfer design point parameters are dependent upon a set of performance parameters defined at different points in the gas turbine thermodynamic cycle, such as inlet conditions, at cycle point no 2, engine core flow, at cycle point no. 2.5, compressor discharge conditions of temperature and pressure, at cycle point no. 3; turbine inlet conditions of temperature and pressure, at cycle point no. 4; high pressure rotor inlet conditions of temperature and pressure, at cycle point no. 4.1; low pressure inlet conditions of temperature and pressure, at cycle point no. 4.5; and high and low rotor speeds for different ambient conditions.

4.4-4 Gas Temperature Transverse Quality

The gas turbine combustor exit gas temperatures are further refined with pattern and profile factors consistent with the burner characteristics[28]. The combustion process that takes place in the burner requires that incoming air be separated into primary and secondary streams for adequate combustion. The primary air is mixed with the fuel at nearly stoichiometric proportions at the center of the burner, and the combustion produces extremely hot core gaseous products. Secondary air is injected from the sides of the combustion chamber and separates the very hot gases from the structure. The secondary air dilutes and cools the products of combustion to acceptable levels before leaving the burner. Because of the size limitations, the burner may not be sufficiently large to give gases time to mix homogeneously, and as a result, the turbine may experience gas temperature variations which give rise to pattern and profile factors[29]:

$$\text{Pattern Factor} = \frac{T_{max} - T_4}{T_4 - T_3} \tag{5}$$

$$\text{Profile Factor} = \frac{T_{mr} - T_4}{T_4 - T_3}, \tag{6}$$

where T_{mr} = maximum circumferential mean temperature.

For the first vane, the peak temperature is obtained from pattern factor and this information is used for thermal-mechanical design. It should be noted current combustor exit temperatures are in excess of 3000°F (1650°C) with expected growth towards 3800°F (2100°C). As the flow passes through the turbine components, the temperature profile retains the same basic form of the high temperature in the center region and lower temperature at the outside region, but it is also affected by the processes that take place during turbine expansion, such as mixing, tip leakage, and development of secondary flows. Figure 4 illustrates the thermal load distribution for the high-pressure turbine components[30]. The primary gas temperature of interest in blade design is the total temperature relative to the blade[31]:

$$T_{gas,\,relative} = T_{gas} - \frac{V^2}{2Jg_c c_p} + r\frac{W^2}{2Jg_c c_p} \tag{7}$$

At the inlet to the rotor, the relative velocity W is smaller than the absolute velocity V, and the relative gas temperature should reflect the effect of Mach number through the recovery factor, $r = Pr^{1/3}$ [32].

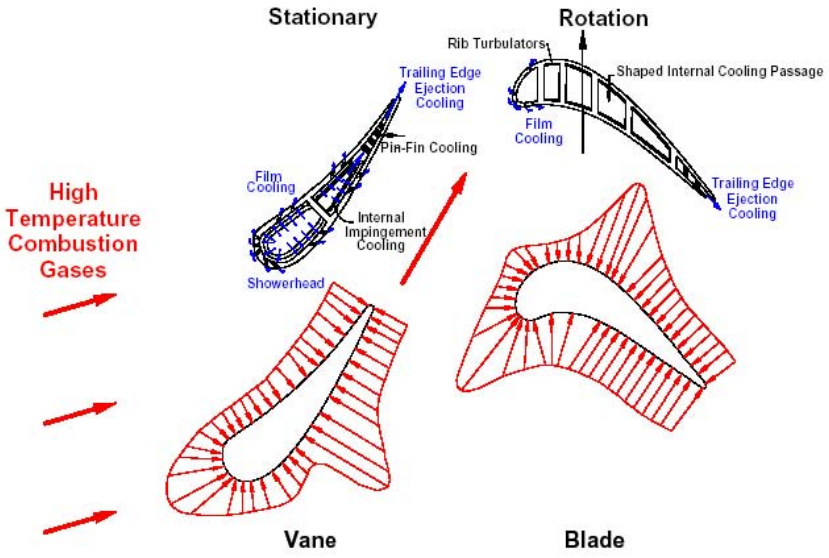

Fig. 4. Illustration of thermal load distribution for the high-pressure turbine components.

Source: See Note 30.

The effect of secondary flows on streamline migration and the effect of film flow should be reflected in the stage Mach number distributions. In addition to these considerations, there are margins or adders that lead to increments imposed on the gas temperature values. These are used to account for the following design tolerances: engine-to-engine variation, deterioration, overshoot, and production scattered tolerance to sustain thrust guarantee[33]. It should be noted that film, or external surface to gas, thermophysical properties required to determine heat transfer coefficients, for instance, should be calculated using Eckert's reference temperature[34]. Other dimensionless ratios used to characterize stage local conditions, such as relative-to-total temperatures and pressures can be assumed nearly constant for operating conditions at idle and above in high-pressure turbine design[35].

4.4-5 Airfoil Thermal Load

Externally to the turbine airfoil, gas static pressure and gas stream velocity distributions are used for determining the external heat transfer coefficients. The external heat transfer depends on the development of the boundary layers on the airfoil. The external boundary layer is subject to several factors, which make this calculation difficult. These factors include, pressure and temperature gradients, turbulence level, surface curvature, surface roughness, laminar-to-turbulent transition, and flow unsteadiness. Separation bubbles near the airfoil leading edge could also have a major influence on the development of the boundary layer. These could be caused by rapidly changing the curvature or during off-design conditions when incidence angles may be high. If, however, pressure gradient is favorable and strong enough, a turbulent boundary may re-laminarize with subsequent reduction in the heat load. It should be noted that the presence of film cooling will invariably trip or energize the boundary layer. Standard relations for flow over flat plate with suitable modifying factors to account for these effects, can be used to calculate external heat transfer rate to the airfoil as follows[36]:

$$\mathrm{Nu}_x = 0.0296\, C_{\text{empirical}}\, \mathrm{Re}_x^{4/5} \mathrm{Pr}^{1/3},$$

$$\text{where} \quad \mathrm{Nu}_x = \frac{h\ x}{k}, \quad \mathrm{Re}_x = \frac{\rho V x}{\mu}, \quad \text{and} \quad \mathrm{Pr} = \frac{\mu}{c_p k} \ . \tag{8}$$

The empirical correlation factor is obtained by matching test data.

Despite their simplicity, the flat plate correlations provide a good estimate of heat transfer. Figure 5(a) and 5(b) are examples for the pressure and suction sides[37]. The Nusselt number calculated are based on measurements of static pressure, from which the distribution of the Reynolds number is obtained. On the downstream region of the suction side, with fully turbulent flow, the heat transfer coefficient is predicted well. On the pressure side, the turbulent flat plate correlation predicts heat transfer well on downstream region towards the trailing edge; but on the upstream region, the heat transfer prediction is low. In this upstream region the flow is very unsteady causing very large heat transfer coefficients. Fortunately, heat transfer coefficients are predicted using boundary layer codes, such as those of reference[38], which account for curvature effects, transition and surface roughness on the airfoil external wall.

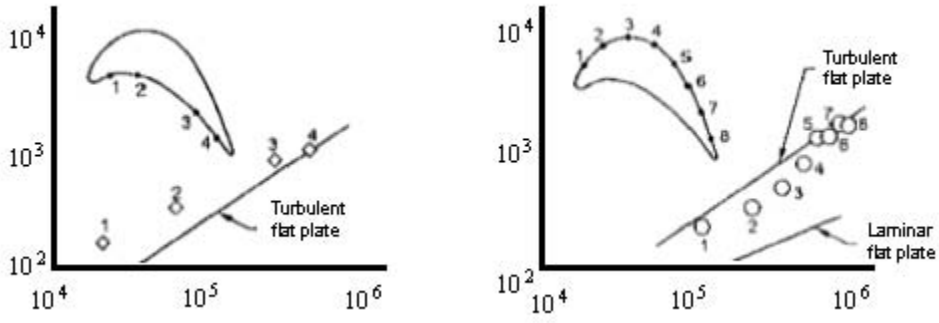

(a) (b)

Fig. 5. Flat plate correlations estimate of heat transfer on the pressure (a) and suction (b) sides of the high-pressure turbine airfoil in terms of Nusselt numbers versus Reynolds numbers.

Source: See Note 37.

Besides, main-body airfoil thermal load calculations, airfoil tip and blade platform thermal loads need to be determined as well. Tip heat transfer is difficult to determine due to the complexities associated with leakage flows over a relatively small gap between rotating blades and stationary shrouds. However, references listed in note 39 can be consulted for determining the external heat transfer coefficients of different tip configurations[39]. Similarly, platform heat transfer is also complex due to the secondary flow and leakage effects associated with inter-segment gaps. In this regard, note 40 can be consulted for determining the external heat transfer coefficients associated with these difficult situations[40].

4.4-6 Leading Edge Thermal Load

At the leading edge, effects related to unsteadiness due to the row of upstream airfoils lead to high heat transfer coefficients and empirical correction factors are usually applied as follows[41]:

$$Nu_{d_{LE}} = 1.14\, C_{empirical}\ Re_{d_{LE}}^{1/2}\, Pr^{0.4}\left[1+\left(\frac{\theta}{90}\right)^3\right] \quad , \tag{9}$$

where all variables are defined in the nomenclature with $0<\theta<80.$

Turbine airfoils are optimized for aerodynamic performance and heat load to improve airfoil life. The ideal heat transfer objectives, during the conceptual airfoil design, include the following considerations: (1) blunt leading edges to minimize heat transfer coefficients at the airfoil stagnation points, (2) minimize blade count to minimize cooling surface. (3) minimal pressure diffusion to minimize separation and high external heat transfer coefficients, (4) increase mid-body airfoil thickness to reduce losses in internal cooling serpentine cooling arrangements, (5) avoid low trailing edge wedge angles that lead to large distances from the trailing edge and the pressure side coolant ejection (film) bleeds. Some of these considerations may be in conflict with aerodynamic objectives, and, in general, a compromise is reached between cooling and aerodynamic design groups.

4.4-7 Coolant Heat Transfer

The overall cooling effectiveness, φ , as a dimensionless metal temperature is a function of the other cooling parameters, such as the convective efficiency, η_c, and the film effectiveness, η_f , for a given heat load, β , to the part . The relationship between these cooling parameters can be expressed in a simple relationship, derived from one-dimensional heat transfer analysis as follows[42]:

$$\varphi = \frac{\beta\eta_c + \eta_f(1-\eta_c)}{1+\eta_c(\beta-\eta_f)} \quad . \tag{10}$$

If a metal temperature at a point in the airfoils is limited to a required value for a specified thermal load, β ; then, the overall cooling effectiveness, φ , as a measure of metal temperature, is set for the design, and the design process begins with a search of the required internal convective efficiency and film effectiveness.

4.4-8 Film Cooling

Film cooling takes the cooling medium and discharges it in a carefully designed pattern of openings in the blade surface to form a protective film over the airfoil surface. This film blanket reduces the external heat load to the airfoil by reducing the driving temperature from the local gas temperature to the film temperature, as shown in Figure 6. The film cooling effectiveness is a function of injection geometry on the airfoil including the hole diameter, d_h , hole spacing, x_n , effective slot height, $s = \pi d_h^{\,2}/(4x_n)$, surface distance from the film row, x, inclination of the film hole axis to the surface in terms of in-plane and out-of-plane angles, blowing parameter, $M = (\rho v)_{coolant}/(\rho v)_{gas}$, density ratio, the ratio of x/(Ms), and film coverage, Cov[43]. Film coverage is a fraction of the length along the row of film holes which is covered by the footprint of the breakout of the holes and is usually given by the ratio of film hole breakout, b, to the film hole pitch, p, or Cov=b/p. Film effectiveness can then be expressed analytically as:

$$\eta_f = \frac{1}{\frac{1}{Cov}+c_1\left(\frac{x}{Ms}\right)^{c_2}} \quad , \tag{11}$$

where, the empirical constants, C_1 and C_2 , are determined by fitting the test data for different film cooling configurations. In general, the exponent C_2 is about the same order of magnitude for the pressure and suction sides of the airfoil. However, coefficient C_1 is about an order of magnitude different between the pressure and suction side of the airfoil with the pressure side film decaying much faster on the pressure side of the airfoil. It should be noted that when the empirical constants of equation (11) are matched with test data, most of the density ratio for the data reported in the literature is about unity, and this data needs adjustment for typical engine environments.

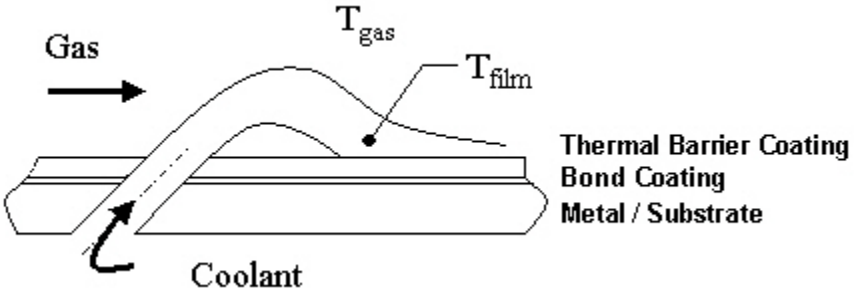

Fig. 6. Film blanket reduces the external heat load to the airfoil by reducing the driving temperature from the local gas temperature to the film temperature.

The use of diffuser shaped holes for film cooling reduce the penalties associated with film of blowing ratios, M. Shaped holes also provide increased coverage, as shown in figure 7[44]. In the past, shaped holes were almost eliminated in favor laser drilled round holes, but it is now apparent that they should be used due to superior cooling advantage over laser drilled holes. For a given coolant flow, laterally averaged film cooling effectiveness from staggered double row of holes is usually higher than from a single row of holes. However, for the same coolant flow, the double row hole diameters may be expensive to make. The injection of coolant from succeeding rows of film holes results in a cooler film temperature than if only one row of holes were blowing. Film temperatures superposition produced by coolant injection from multiple rows of film holes can be evaluated by successive heat balance stations. This procedure is repeated for blowing from all N successive rows of holes upstream of the heat balance station as follows[45]:

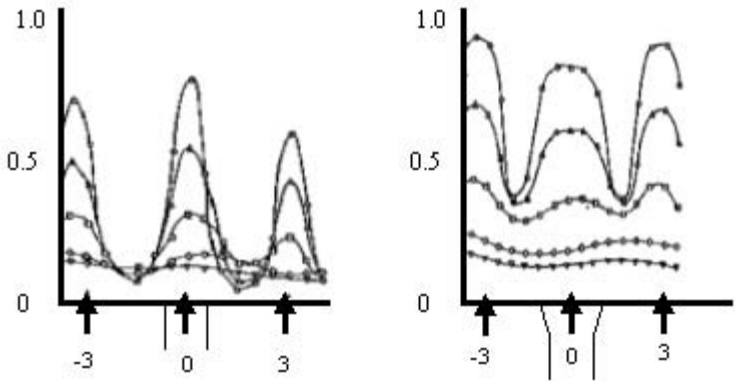

Fig. 7. The use of diffuser shaped holes for film cooling provide increased film coverage in terms of film effectiveness versus hole locations.

$$\eta_f = \sum_{i=1}^{N} \eta_{f_i} \left[\prod_{j=0}^{i-1} (1 - \eta_{f\,j}) \right] \quad . \tag{12}$$

Computer programs are developed to superimpose the film cooling effectiveness distribution downstream from several rows of film holes having individual levels of coolant injection, temperature, and flow rate to provide the effective distribution of cumulative film cooling effectiveness; and, hence, film temperature along the airfoil surfaces.

4.4-9 Trip Strips or Turbulence Promoters for Cooling Passages

If the film effectiveness, η_f , is known for a particular design, due to the number and arrangement of film cooling holes; then the only unknown in equation (10) is the convective efficiency, η_c . This convective efficiency has a fundamental solution, which can be given, in simple terms, by the relation:

$$\eta_c = 1 - e^{-\frac{h_c A_c}{m\, c_p}} \quad . \tag{13}$$

In this expression, the convective efficiency, η_c , is related to the internal heat transfer coefficient, wetted surface area, and coolant flow rate. Expression (13) allows for design features to be evaluated in terms of this performance parameter. That is, for a required convective efficiency, η_c , limited by the required cooling effectiveness, φ ; then a required product of internal heat transfer coefficient with the wetted surface area, $h_c A_c$ can be evaluated as a fundamental requirement for the cooling design.

In a general, it is the goal of the design to obtain the largest $h_c A_c$ product, for the least amount for coolant flow rate, m , possible. Insofar as the airfoil internal cooling features are concerned, there may be a large number of configurations that can be explored in the design space as noted in the reference provided by Han, et al.[46]. These would include configurations with internal cooling features, such as pedestals or turbulating trip strips just to mention just a few.

Patankar and Spalding observed that in the near the internal wall of the airfoil, the convection associated with the primary flow direction can be neglected, the so-called Couette flow assumption[47]. However, for the specific case of predicting the boundary layer behavior under the influence of rotation, this assumption may not be applicable. The boundary layer equations for momentum and energy can be written as:

$$\tau = \tau_w + m'' v + \frac{dp}{dx} y \tag{14}$$

$$q = q_w + m'' c_p (T - T_w) \quad . \tag{15}$$

The first term of the right-hand-side of equation (14) represents the shear stress at the wall. The second term represents the crosswise convective mass flux, where the velocity is taken as the mean velocity component normal to the wall, in the near wall region. This cross-wise component exists due to rotational Coriolis influences on the boundary layer. The third term represents the axial pressure gradient on the boundary layer. The variable, y, is taken as the cross-stream coordinate away from the wall. All other symbols are provided in the nomenclature.

The relations given by equations (14) and (15) are written in dimensionless form by using the traditional groups of v^+ , y^+, and p^+ defined in the nomenclature. When these groups are substituted into (14) and (15), the following new relationships are obtained;

$$\tau^+ = 1 + m^+ v^+ + p^+ y^+ \tag{16}$$

$$q^+ = 1 + m^+ T^+ . \tag{17}$$

Using the diffusion laws, the effective (laminar and turbulent) shear stress and heat flux are written in dimensionless form as

$$\tau^+ = \frac{\mu_e}{\mu}\left(\frac{dv^+}{dy^+}\right) \tag{18}$$

and

$$q^+ = \frac{\mu_e}{Pr_e \mu}\left(\frac{dT^+}{dy^+}\right), \tag{19}$$

where μ is the dynamic viscosity, μ_e is the effective viscosity, and Pr_e is the effective Prandtl number.

Two ordinary differential equations describing momentum and energy transport in the boundary layer can be obtaining by equations (16) and (17) with equation (18) and (19), respectively. If the mixing-length hypothesis is used for the viscosity ratio as , as $\mu_e/\mu = 1 + (\kappa y^+)^2 \left[1 - \exp(-y^+\sqrt{\tau^+}/A^+)\right] dv^+/dy^+$, described by Crawford and Kays[48], the resulting set of equations become

$$\frac{dv^+}{dy^+} = \frac{2\tau^+}{1 + \left\{1 + 4\kappa^2 y^{+2} \tau^+ \left[1 - \exp\left(-y^+ \tau^{+1/2}/A^+\right)\right]^2\right\}^{1/2}} \tag{20}$$

$$\frac{dT^+}{dy^+} = \frac{(1 + m^+ T^+) Pr_T}{\frac{Pr_T}{Pr} + \left\{\kappa^2 y^{+2}\left[1 - \exp\left(-y^+ \tau^{+1/2}/A^+\right)\right]^2\right\}\frac{dv^+}{dy^+}} \quad , \tag{21}$$

where the effective sub-layer A^+=26 was used proposed by White[49]. The boundary conditions are: $v^+ = T^+ = 0$, at $y^+ = 0$. Equations (20) and (21) can be solved numerically for given Prandtl numbers to yield the desired profiles for the velocity and temperature near the wall. Typical results are succinctly summarized as the law of the wall correlations:

$$v^+ = \frac{1}{\kappa} \ln(E y^+) \tag{22}$$

and

$$T^+ = Pr_T \ (v^+ + P) \quad , \tag{23}$$

where, E and P can be regarded as constant factors for a smooth wall condition and given Prandtl numbers. These are used to calculate the Stanton number at the wall, which is given by the relation:

$$St = \frac{1}{T^+ v^+} \quad . \tag{24}$$

Note that the Nusselt number is related to the Stanton number by the relation; Nu =(Re) (Pr) (St). Solutions (22) through (24) are applied for smooth channels; however, these correlations have been modified to account for non-smooth roughened walls. Typical representations of dimensionless velocity and temperatures have catalogued by Han for a series of configurations[50]. These relationships can assume the form

$$v^+ = -\frac{1}{\kappa} + \frac{1}{\kappa} \ln \frac{d_h}{2e} + R(e^+) \tag{25}$$

and

$$T^+ = [v^+ - R(e^+)] + G(e^+, Pr). \tag{26}$$

The functions R and G are the momentum and thermal roughness functions determined experimentally. All other variables are described in the nomenclature.

In blade cooling passages, repeated roughness elements in the form of regularly spaced ribs are used to increase heat transfer rates. As a by-product of the desired increases in heat transfer rates, the pressure losses through the channel also increase. It is usually necessary to determine the best combination of heat transfer rate increases with the lowest possible pressure losses. As an example, several trip strips configurations in a cooling channel are shown in figure 8. These are described as follows:

(a) Parallel 90 degree ribs
(b) Parallel inclined ribs
(c) Parallel v-shaped (Chevron) ribs
(d) Criss-crossed inclined ribs

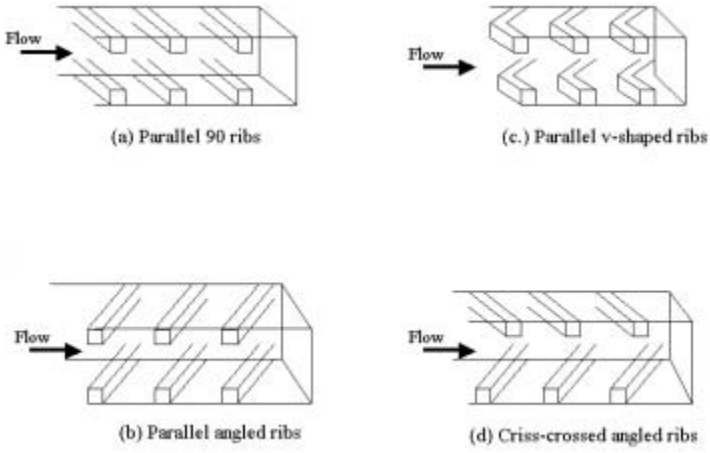

Fig. 8. Several trip strips configurations in cooling channels.

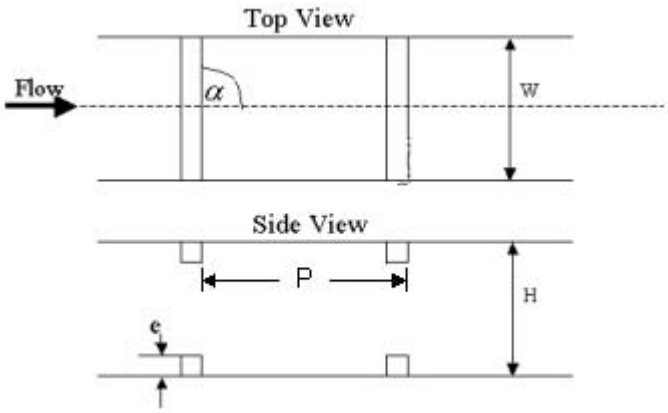

Fig. 9. Illustrates the geometrical parameters for the trip-strip configurations.

The pertinent parameters to consider include the dimensionless heat transfer coefficient, the Stanton Number, the friction factor, and the thermal performance index. Figure 9 illustrates the geometrical parameters for the trip-strip configurations.

The ribbed channel pressure losses were originally modeled using the "law of the wall" similarity by Nikuradse for sand grain roughness[51]. The correlating parameter became known as the roughness function, R, which, for rectangular channels, is defined as:

$$R = \sqrt{\frac{2}{f}} + \frac{1}{\kappa} \ln\left(\frac{2e}{d_h}\right) + \frac{1}{\kappa} \tag{27}$$

where: e is the rib height, f is friction factor, and d_h is the channel hydraulic diameter. The friction factors and the roughness function for the rib configurations (a)-(d) of figure 8 are given in Table I.

Table I. Friction factor and momentum roughness function for the configurations of Figure 8.

	Friction factor	Roughness function
A	$f = \frac{W}{W+H}\left\{\frac{H}{W}f_S + \frac{2}{(R - 2.5\ln(2e/d_h) - 2.5)^2}\right\}$ f_S = Smooth friction factor = $0.046Re^{-0.2}$ W = Channel width H = Channel Height	$R = 3.2(\frac{p/e}{10})^{0.35}$
B	$f = 2\left\{R - [2.5\ln(2e/d_h) + 2.5]\right\}^{-2}$ $e^+ = \frac{e}{d_h} Re\sqrt{f/2}$ n = 0 for $\alpha \geq 45$ $n = 0.17$ *for* $\alpha < 45$	$R = [(\frac{p/e}{10})^{0.35}(.003e^+)^n$ $[15.6 - 31.6(\frac{\alpha}{90^\circ} + 21.1(\frac{\alpha}{90})^2]$
C	$f = \frac{1}{2}f_S + \left\{R - [2.5\ln(2e/d_h) + 2.5]\right\}^{-2}$	$R = ae^{+b}$ a = 1.605 b = 0.0015 for α = 45 p/e = 10 a = 1.232 b = 0.0454 for α = 60 p/e = 10 a = 3.687 b = −0.0571 for α = 60 p/e = 20 $e^+ = \frac{e}{d_h} Re(\frac{2f - f_S}{2})^{1/2}$
D	$f = \frac{1}{2}f_S + \left\{R - [2.5\ln(2e/d_h) + 2.5]\right\}^{-2}$	$R = 3.18$ $e^+ = \frac{e}{d_h} Re(\frac{2f - f_S}{2})^{1/2}$

Sources:

(a) See Note 52.

(b) Han, J.C., J.S. Park, and C.K. Lei, "Heat transfer enhancements in channels with turbulance promoters", Trans. ASME J. Eng. Gas Turbine and Power, Vol. 107, 628-635,1985.

(c) Han, J.C., Y.M. Zhang and V.P. Lee, "The influence of surface heat flux ratio on heat transfer augmentation in square channels with parallel, crossed and V-shaped angled ribs", ASME Paper 91-GT-3, 1991.

(d) Lau, S.C., R.T. Kukreja and R.D. McMillin, "Effects of V-shaped rib arrays on turbulent heat transfer and friction of fully developed flow in square channel", Int. J. Heat Mass Transfer 34, 7, 1605-1616, 1991.

Using the Reynolds analogy between momentum and heat transfer, Dipprey and Sabersky developed a thermal analog to the roughness function to correlate heat transfer data in sand roughened channels[52]. Webb et al., extended the analysis to rib roughened channels[53]. The thermal roughness function was given by:

$$G = R + \frac{\frac{f}{2St} - 1}{\sqrt{\frac{f}{2}}} \tag{28}$$

The corresponding heat transfer correlations for geometries (a) – (d) of figure 8 are given in Table II.

Table II. Stanton Number and thermal roughness function for the configurations of Figure 8

	Heat Transfer Correlations	Thermal Roughness Function
A	$St_r = \frac{f/2}{\sqrt{f/2}\,(G-R)+1}$	$G = 3.7e^{+0.28}$
B	$St_r = \frac{f/2}{\sqrt{f/2}\,(G-R)+1}$	$G = (\frac{p/e}{10})^{0.14} 2.83 (\frac{\alpha}{90})^{0.3} e^{+0.28}$
C	$St_r = \frac{((2f-f_S)/2)^{1/2}}{G-(2.5\ln(2e/d_h)+2.5}$	$G = ae^{+b}$ $a = 1.819$ $b = 0.355$ for $\alpha = 45$ $p/e = 10$ $a = 1.299$ $b = 0.399$ for $\alpha = 60$ $p/e = 10$ $a = 1.685$ $b = 0.376$ for $\alpha = 60$ $p/e = 20$
D	$St_r = \frac{((2f-f_S)/2)^{1/2}}{G-(2.5\ln(2e/d_h)+2.5}$	$G = 1.82\ e^{+0.41}$

Sources:

(a) See Note 52.

(b) Han, J.C., J.S. Park, and C.K. Lei, "Heat transfer enhancements in channels with turbulance promoters", Trans. ASME J. Eng. Gas Turbine and Power, Vol. 107, 628-635,1985.

(c) Han, J.C., Y.M. Zhang and V.P. Lee, "The influence of surface heat flux ratio on heat transfer augmentation in square channels with parallel, crossed and V-shaped angled ribs", ASME Paper 91-GT-3, 1991.

(d) Lau, S.C., R.T. Kukreja and R.D. McMillin, "Effects of V-shaped rib arrays on turbulent heat transfer and friction of fully developed flow in square channel", Int. J. Heat Mass Transfer 34, 7, 1605-1616, 1991.

The motivation for placing the ribs in a channel is to increase the rate of heat transfer from the channel walls to the bulk fluid. This is accomplished by two distinct mechanisms. First, the placement of ribs act as turbulators to break-up the near wall flow increasing the turbulence level and enhancing the exchange of fluid in the near wall region with the core flow by action turbulent diffusion. While this increases the heat transfer, it also increases the wall friction resulting in higher pressure losses. A second heat transfer mechanism is active if the ribs are inclined to the core flow direction. In this case, the ribs induce secondary flows in the core flow, which can circulate fluid from the middle of the channel towards the walls thus increasing the heat transfer along these walls. The secondary flows have a smaller effect on the pressure losses, thus they are more beneficial of increasing the thermal performance of the cooling channel.

The flow in a ribbed channel can be divided conceptually in a main core flow and near wall flow. The flow structures that have been observed in the vicinity of the ribbed wall are shown in Figure 10[54]. This structure varies primarily upon the geometrical ratio of p/e. As an example, when p/e>7, three different separated flows regions are observed: (1) In front of the rib, a separated

recirculation zone exists; (2) on top of each rib a separation bubble forms due to upstream facing step; (3) following the back side of the rib, a separated recirculation region exists which can extend up to 7 rib heights downstream before the flow reattaches. From this point the boundary layer re-develops until the next separated region is encountered upstream of the rib. When p/e<7, the two separated regions which lie between the pair of ribs combine. On top of each rib a separation bubble exists. When p/e=7, the boundary layer between the separation zones and preceding the up and downstream ribs does not have a chance to develop. Separation occurs on the top of each rib. When p/e=10, the separation bubble at the top of the rib may not re-attach on the top surface of the rib but it may extend past the back of the rib and combine with the separation region following the rib. The re-attachment occurs between ribs. This is believed to be the optimum configuration. However, the effects of the Reynolds number may determine the validity of these results.

The core flows develops rapidly in a ribbed channel compared to a smooth one. Friction factors become constant after the 3rd rib or 4 diameters downstream. The Nusselt number shows similar behavior. The presence of the ribs increase turbulence and induce secondary flows that tend to move fluid from the main core towards certain walls and away from the others. Similar core fluid flow and heat transfer enhancements are found in rotating channels caused by Coriolis as illustrated in figure 11. This is particularly true for channels with aspect ratio of unity. Sources listed in note 55 can be consulted for determining the effects of rotation on internal heat transfer coefficients where rotational and buoyancy numbers are the fundamental dimensionless parameters[55]. The thermal performance can be defined by the parameter of $St/f^{1/3}$ as given by Webb and Eckert[56]. It relates the heat transfer to friction factors or pressure loss in the channel.

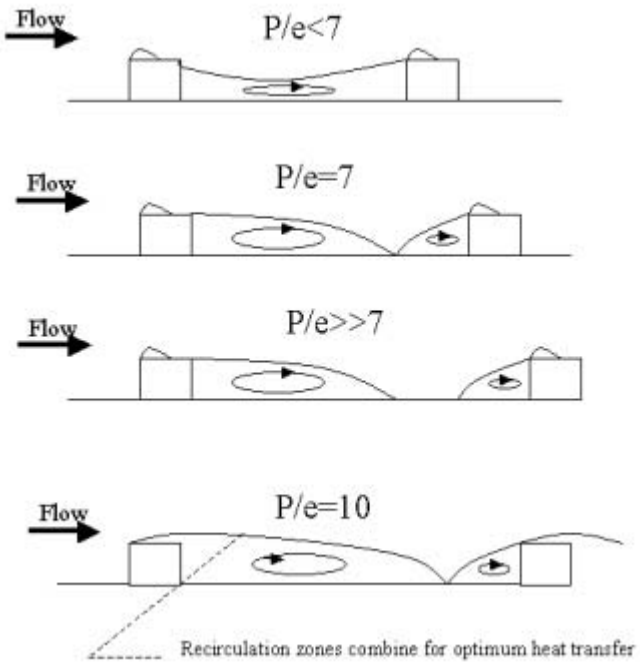

Fig. 10. Observed flow structures in the vicinity of the ribbed wall.

Source: See Note 53.

4.4-10 Impingement Cooling for Cross-Over Holes and Inserts

The impingement configurations have been used extensively in the gas turbine industry. In general, there are two locations in airfoil design where impingement cooled has been used. The first location is used for leading edge cooling. Dedicated cooling air is allowed to pass through rib cross-over openings leading to jet impingement on the inner wall of the airfoil leading edge[57]. After impingement cooling the air flow passes through a series of film holes forming a shower-head arrangement through the airfoil the leading edge. Internal jet impingement, convective cooling through the film holes, and film cooling become very effective means to cool this section of the airfoil with very high heat loads. The other location is for trailing edge cooling. In this case, the cooling air is allowed to pass through a series of rib cross-over openings[58]. Jet impingement occurs after each cross-over hole. The air impinges on each subsequent ribs and surrounding walls before discharging at the trailing edge exit slots. Many references can be consulted for obtaining impingement heat transfer coefficients for these two configurations[59].

For high-pressure vanes, inserts or baffles can be used to cool the airfoil with impingement cooling. There are several references that can be consulted in this regard[60]. Each impingement correlation for this type cooling will be dependent on the cross flow degradation from upstream impingement jets. A useful correlation has been provided by Floerschuetz et al as follows[61]:

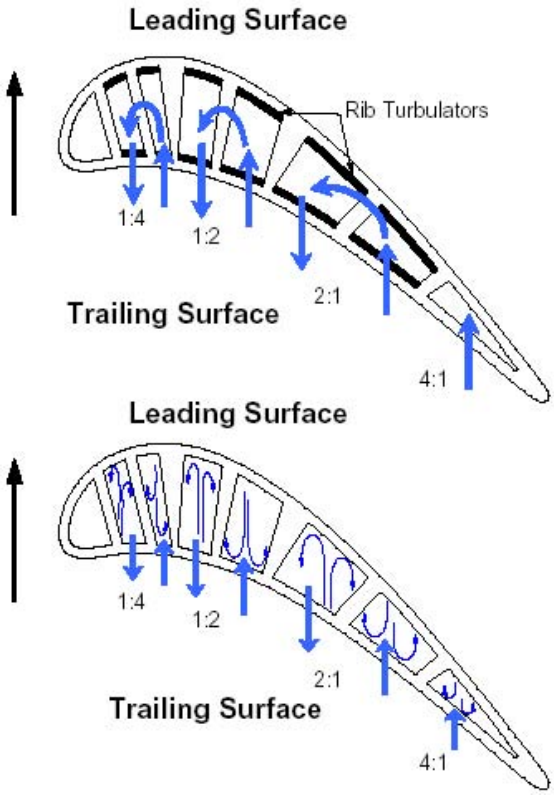

Fig. 11. Core fluid flow and heat transfer enhancements are found in rotating channels caused by the rotating vortices inside the cooling passages.

Source: See Note 30.

$$Nu = ARe_{d_j}{}^{m}\left[1 - B\left(\frac{z_n}{d_j}\frac{(\rho\, v)_c}{(\rho\, v)_j}\right)^{n}\right]Pr^{1/3} \quad ,$$

$$A,\quad B,\quad m,\quad n = C\left(\frac{x_n}{d_j}\right)^{n_x}\left(\frac{y_n}{d_j}\right)^{n_y}\left(\frac{z_n}{d_j}\right)^{n_z} \tag{29}$$

where

	C	n_x	n_y	n_z
A	1.180	-0.944	-0.642	0.169
M	0.612	0.059	0.032	-0.022
B	0.437	-0.095	-0.219	0.275
N	0.092	-0.005	0.599	1.040

The different variables are described in the nomenclature. The validity of correlation is the defined by the following parameter range:

$$1 \le \frac{z_n}{d_j} \le 3;\quad 1 \le \frac{x_n}{d_j} \le 15;\quad 4 \le \frac{y_n}{d_j} \le 6;\quad 0 \le \frac{v_c}{v_j} \le 0.8;\quad \text{and}\quad 5000 \le Re_{d_j} \le 50{,}000$$

It should be noted that for the calculation of the Reynolds number in correlation (29) needs to be determined for the flow passing through the insert impingement holes. Flow through these openings is a result of pressure differences which can be obtained from an overall flow network analysis.

4.4-11 Pin-Fin or Pedestals for Trailing Edge Cooling

In trailing edge designs, typically two rows of cross-over holes are used for cooling. The flow acceleration is high through these cross-over impingement openings. The coolant flow Mach number profiles follows that of the coolant static pressure profile in that it assumes almost step-wise profiles as the cooling flow crosses through these openings. The step-wise profiles are undesirable as they lead to relative high peaks in internal heat transfer coefficients at the walls of the blade as illustrated in figure 12. In other words, there are regions in the airfoil trailing edge walls, which attain relative lower metal temperatures due to high internal heat transfer coefficients. Meanwhile, other areas attain relatively higher metal temperatures due to lower internal heat transfer coefficients. These metal temperature differences can lead to high thermal strains, which in conjunction with transient thermal response during take-off or power loading can, in turn, lead to undesirable thermal-mechanical fatigue damage.

It is, therefore, desirable to use a trailing edge cooling design, which improves the internal profiles for Mach number, static pressure drop, and internal heat transfer coefficient distributions along the airfoil trailing edge. In that regard, internal features, such as pedestals provide design advantages. Optimum designs may include internal pedestals with many different cross-sectional areas, such as: circular, oval, racetrack, square, rectangular, diamond cross-sections, just to mention only a few. In the illustrative example that follows, attention is given to the most simplest form of an internal cooling feature: such as round pedestals.

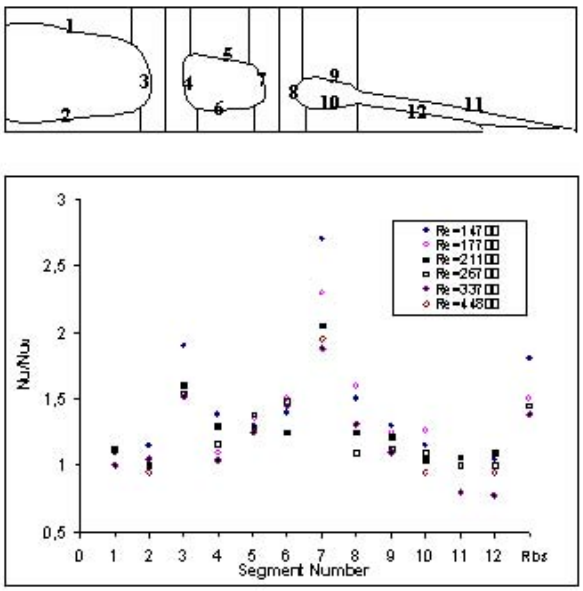

Fig. 12. Localized heat transfer enhancement on different segments in trailing edge cavities.

Source: See Note 58.

The relevant cooling characteristics of round pedestals could easily be extended to other cross-sectional area pedestals for specific applications. In this context, for a staggered array of round pedestals the internal unobstructed trailing edge channel area will have a cross-sectional area, A=WH, where W is the width and H is the channel height. The corresponding perimeter becomes Per = 2 (W+H) , and the hydraulic diameter is given by $d_H = 4A/Per$. The surface area becomes $A_{duct} = 2WL$, where L is the length of the channel. The surface of the plate not being covered by the pedestals becomes $A_{plate} = A_{duct} - 2(N_L N_T)[\pi(d_{pin}{}^2/4)]$, where N_L and N_T are the number of pedestals in the longitudinal and transverse directions of the trailing edge channel. It should be noted that the number of pedestals can be given by $N_T = W/S_n$ and $N_L = L/S_p$, where S_n and S_p are the transverse and longitudinal pitches, respectively. With these geometrical parameters, the Reynolds number, associated with the pin diameter, is calculated as follows: $Re_d = \rho d_{pin} V_{max}/\mu$, where $V_{max} = V(A/A_{min})$ with $A_{min} = (W - N_T d_{pin})H$. In this case, the coolant velocity, V, is the free stream inlet velocity. With the knowledge of the pin Reynolds number, the following relationships for the Nusselt number from table III can be obtained, following Zukauskas[62].

Table III. Pedestal Nusselt numbers [17].

$Re_d > 200{,}000$	$Re_d > 200{,}000$	$Re_d \le 200{,}000$	$Re_d \le 200{,}000$
$Pr > 1$	$Pr \le 1$	$Pr \le 1, S_n/S_p > 2$	$Pr \le 1, S_n/S_p \le 2$
$Nu_{pin} = 0.022 Re_d{}^{0.84} Pr^{0.366}$	$Nu_{pin} = 0.019 Re_d{}^{0.84}$	$Nu_{pin} = 0.40 Re_d{}^{0.6} Pr^{0.36}$	$Nu_{pin} = 0.35\left(\frac{S_n}{S_p}\right)^{0.2} Re_d{}^{0.6} Pr^{0.36}$

For the area not affected by the pedestals, the plate Nusselt number is given by $Nu_{plate} = 0.077 Re_d{}^{0.70}$ [63].The pin fin efficiency is obtained from the relationship Ishida et al [65]:

$$\eta_{pin} = \left(\frac{d_{pin}}{H}\right)\left(\frac{\beta_k}{Nu_{pin}}\right)^{0.5} \tanh\left[\left(\frac{Nu_{pin}}{\beta_k}\right)^{0.5} \frac{H}{d_{pin}}\right] \quad , \tag{30}$$

where all variables are described in the nomenclature.
The overall internal heat transfer with pedestals is then based on the following two contributions: (1) the plate contribution, and (2) the pin contribution as follows·

$$Nu_d = \left(\frac{A_{plate}}{A_{duct}}\right) Nu_{plate} + \eta_{pin}\left(\frac{A_{pin}}{A_{duct}}\right) Nu_{pin} \quad . \tag{31}$$

The corresponding heat transfer multiplier, HM, normalized by the Dittus-Boelter correlation[64], $Nu_0 = 0.023 Re_H{}^{0.8} Pr^{0.4}$, is then given by

$$HM = \left(\frac{Nu_d}{Nu_o}\right)\left(\frac{d_H}{d_{pin}}\right) \quad . \tag{32}$$

The pressure drop calculations through a bank of pedestals is given by Ishida et al. and are presented here for completeness as follows [65].

$$\Delta P = (4f)\left(\frac{\rho V_{max}{}^2}{2}\right) N_L$$

$$\text{where} \quad f = \left(\frac{2.132}{Re_d\left(4\frac{S_n}{d_{pin}} - 1\right)}\frac{d_{pin}}{H} + \frac{0.872}{Re_d{}^{0.278}}\right) \quad . \tag{33}$$

The corresponding friction multiplier, FM , normalized with Blasius resistance formula, $f_0 = 0.316/Re_H^{0.25}$, becomes

$$FM = \frac{4f\left(\frac{d_H}{L}\right)\left(\frac{W}{W - N_T d_{pin}}\right)^2 N_L}{f_o} \tag{34}$$

Relationships provided by equations (32) and (34) can be used to design a trailing edge cooling channel with round pin-fins. These were provided here to represent a design procedure; however, many other empirical correlations can be obtained for other type of internal features as described by Han et al.[66]. The overall procedure for obtaining heat transfer and friction multipliers would follow the steps outlined here. In many instances, plots of FM/HM versus Re_H are used to compare the performance of different configurations. One such plot is shown in figure 13, based on mass-transfer augmentation, from Chyu[67]. By mass-transfer to heat transfer analogy, the results of this plot are directly related to heat transfer assessment. Figure 13 allows for comparison and determination of which configuration would provide the best heat transfer for the least pressure drop. Plots similar to that of figure 13 are usually called performance index plots and become useful early in the design process.

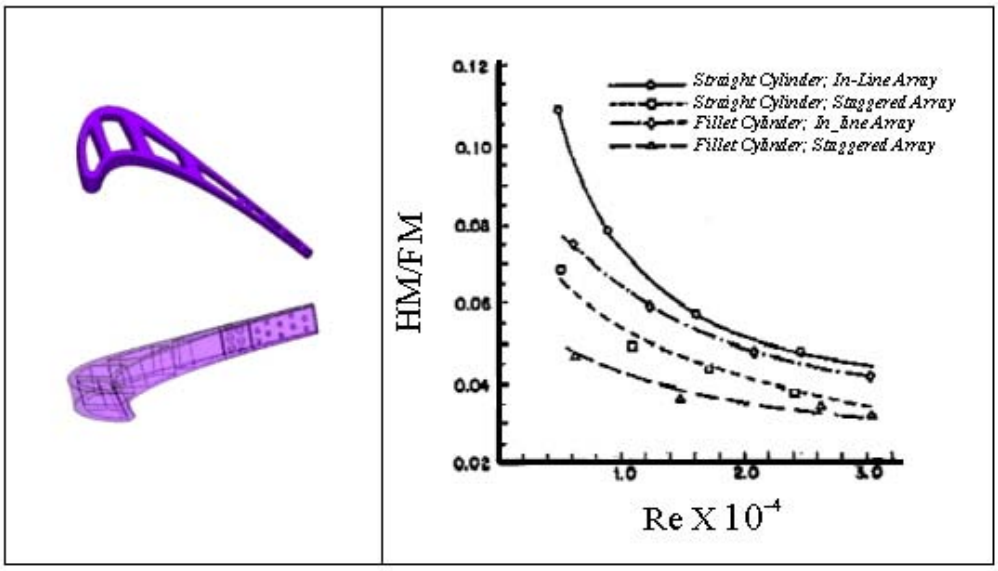

(a) (b)

Fig. 13. Pedestal trailing edge configuration and test results; (a) transparent view of blade showing pedestal bank at trailing edge (b) effect of Reynolds number on performance index (HM/FM) in straight pins with fillets.

Source: See Note 20.

4.4-12 Bulk Temperatures for Cooling Passages

To estimate airfoil cavity cooling flow, one needs to consider the inlet coolant flow rate, at the root of the blade passage, denoted here as m_{Root}, as well as the cooling flow rate at the several film holes, denoted as m_{film}, and flow variation through the cavity. The linear function of cooling flow rate distribution from the root as flow exits the airfoil cavity leads to the following flow relationship[68]:

$$m(r) = m_{Root}(1 - ar)$$

$$\text{where} \quad a = \frac{1}{L_H}\left(1 - \frac{m_{film}}{m_{Root}}\right). \tag{35}$$

with L_H as the blade span radial height to the film hole location. The temperature of the coolant inside the cavity is obtained by considering an infinitesimal small control volume, dr, in the supply cavity. This consideration leads to the following energy balance[69]:

$$mc_P \frac{dT_c}{dr} = \frac{dQ}{dr} + \frac{mr\omega^2}{Jg_c} \quad , \tag{36}$$

$$T_c(r) = T_{c,Root} + \left(\frac{Q}{aL_H m_{Root} c_p} \right) \ln\left(\frac{1 - ar_{Root}}{1 - ar} \right) + \frac{(r^2 - r_{Root}{}^2)\omega^2}{2Jg_c c_p} \tag{37}$$

where Q denotes the total heat transfer onto the corresponding section of radial span, L_H. The coolant flow rate is then introduced in equation (36). The resulting expression is integrated from root to a radial section of the airfoil. This yields an expression for the coolant temperature increase in terms of heat transfer, and rotational pumping, as a function coolant flow rate. The result is:

4.4-13 Thermal-Mechanical Aspects of Durability

Once the internal and external heat transfer loads have been assessed, the gas and coolant temperatures, together with the internal and external heat transfer coefficients, will form a set of boundary conditions for a heat conduction analysis to predict the metal temperatures and stresses in the airfoil. Usually, this analysis begins with the modeling of a 3D section of the blade as a solid model and then proceeds by using a finite element code, such as ANSYS[70], for completing the thermal-stress analysis. An example is provided here for illustrative purposes. It was taken from the NASA report[71] for the E^3 HPT blade. The blade solid model and the corresponding finite element ANSYS model are shown in figure 14. As can be seen from the transparent solid model of figure 14, this blade is cooled by convection with cavity wall trip strips, not shown, and with a set of pedestals in the trailing edge. While external surfaces are locally film cooled from the leading edge with three rows of showerhead holes, there are no film cooling holes on either the pressure or suction surfaces of the airfoil. The trailing edge has a centerline cooling flow ejection.

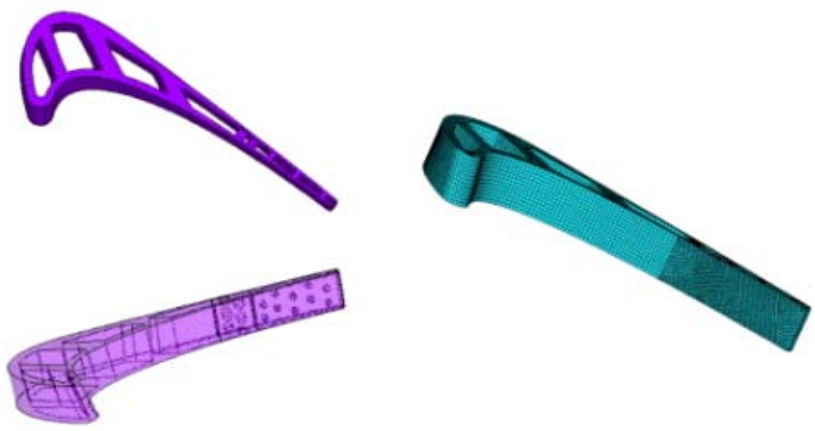

Fig. 14. NASA E^3 blade solid model and the corresponding finite element ANSYS model.

Source: See Note 23.

The NASA E^3 HPT blade is used as a vehicle to demonstrate the thermal-mechanical analysis for a typical uncoated anisotropic turbine component. The 3D model of figure 14, using ANSYS, is composed of 21567 elements, 13494 of which are 3D-10 node tetrahedral structural solid elements in the trailing edge, while 8073 are 3D-20 node structural solid elements in the rest of the airfoil. This hybrid finite element model was selected to improve the meshing of the pedestals in the trailing edge region of the airfoil. This modeling technique is common in durability assessment of turbine airfoils.

The thermal boundary conditions set-up for a blade model is a very laborious process. On the external side, computational fluid dynamic codes can be used to set-up external pressure and Mach number distributions for free-stream conditions with specified turbulence intensity levels. Boundary layer programs are used to establish the external heat transfer coefficients based on expected wall roughness. Gas recovery temperatures and film cooling effectiveness, usually obtained from previous testing, are used to determine the adiabatic wall (film) temperatures. In the end, external heat transfer coefficients and film temperatures are specified as external boundary conditions for the model. Inside the airfoil, flow network models are used to determine internal pressure drops and Mach number distributions.

Heat transfer correlations, based on previous testing, can be used to determine the internal heat transfer characteristics of the blade cooling system under the effects of rotation. Thus, the network flow analysis provides the means to determine internal heat transfer coefficients and coolant temperatures as internal boundary conditions for the model. The thermal results are shown in figure 15, which illustrates a region on the suction side with high metal temperatures corresponding to high thermal loads due to flow acceleration.

In this example selected for illustrative purposes, the mechanical boundary conditions for the model are such that the bottom plane must remain fixed in the direction of the blade stacking axis or the z-direction. One node near the middle of an aft internal rib remains fixed in space for all three directions, and one other node near the leading edge is fixed in the y-direction. The top plane nodes are constrained to remain coupled and planar. The primary crystal coordinate system has the z-axis coincident with pull direction of the centrifugal force experienced by the blade at rated design speed. In order to simulate this, a uniformly distributed load is applied normally to the top face of the blade section. The planar boundary condition applied this way is a first approximation to boundary conditions that may be experienced by the blade section. The assumption is that there is sufficient constraint of the surrounding blade material to counteract bending moments seen as a result of temperature gradients and non-uniform deformation rates[72]. The blade deformation will largely be controlled by the conditions at the ends of the blade. At the root, the blade will experience a relatively lower and more uniform temperature. Thus, if the root of the blade experiences a more uniform temperature, any other cross-section will be forced to deform at a uniform rate[73]. Therefore, to a first approximation, the constraint of planar sections has been applied in the blade model. The results of this structural analysis are shown in figure 16 in terms of von Mises total strains. It should be noted that the analysis provided here could be applied to a more complex blade model as well. The strain results can be used for fatigue assessments. In general, strain range versus cycles to crack initiation are available for the material under consideration leading to assessment of the airfoil fatigue life.

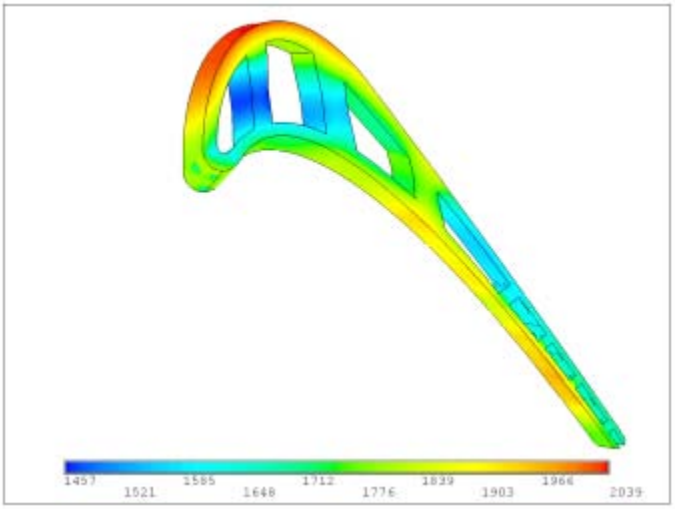

Fig. 15. NASA E^3 blade thermal results.

Source: See Note 23.

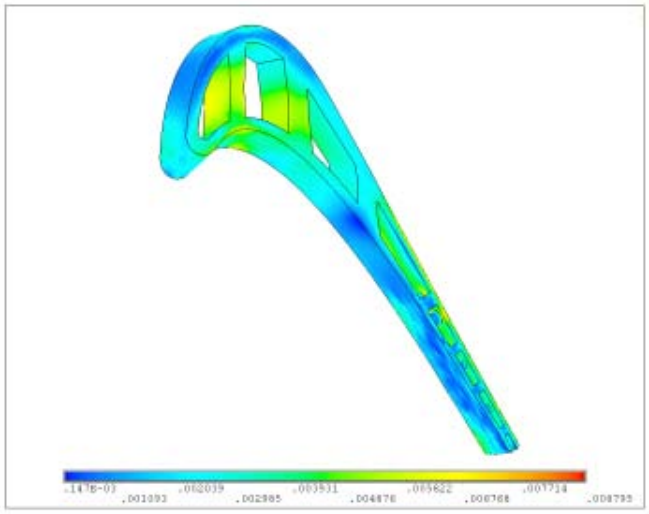

Fig. 16. NASA E^3 blade thermal strain results.

Source: See Note 23.

The allowable stress in the blade depends on its temperature and the target life. The link between these considerations is the behavior of the blade material in creep. Although the maximum stress occurs at the root, this airfoil section may not be the most critical area for creep life. This is because even though the stress may largest at the root, the metal temperature is the lowest. The critical section is then where combination of stress and temperature will make the blade reach the creep limit first. References listed in note 73 present approaches to take the combination of metal temperature and stress in assessing the creep life[74]. For aircraft propulsion engine mission cycles are characterized by takeoff, climb, cruise; whereas for power-generation engine the mission cycle is simpler with long periods of running at constant conditions between starts and stops. At each segment of the mission cycle, the engine will run at different speed and temperature conditions, so that the overall life needs to be considered as the cumulative effect of the life expended in each mission segment. For each set of conditions, a thermal and structural analysis needs to be made, and the results, together with material data, will be used to estimate the creep life of the component.

When the turbine airfoil is subjected to repeated loads, the airfoil may incur fatigue damage[75]. Whereas creep occurs through initially elastic and plastic bulk deformation of the material, fatigue starts at localized plastic points due to defects, inclusions, corrosion and oxidation damage. As soon as cracks exist in the component, the stress is transferred to the remaining material through load shakedown. Eventually, if cracks reach critical size sound material will not be sufficient to support the load leading to failure. As a result, crack initiation, and not propagation, is the preferred way to design for fatigue. In general the total strain, similar to the strain distribution of figure15, can be used with material data to determine the number cycles that the component can withstand. This leads to the concept of damage, D, which is defined as the mission actual cycles relative to the material cyclic capability under the same operating conditions. The overall damage is the accumulated sum of the damage from all flight segments or types. The same definition can be applied for creep damage; but instead of cycles, actual hot time becomes the variable. In the end, the total damage of participating modes should be less than unity as described by the following damage summation equation:

$$\sum_{k=1}^{\text{Overall Mission Cycle}} \left\{ \sum_{i=1}^{\text{Fatigue Cycles}} D_{\text{Fatigue}} + \sum_{i=1}^{\text{Creep Load Cycles}} D_{\text{Creep}} \right\} = 1 \quad (38)$$

There are other relevant modes of damage, such as high cycle fatigue, corrosion, and oxidation; but discussion of these topics would be beyond this subject matter. Suffice to say that metal temperature, steady and unsteady stresses for the turbine component are extremely relevant for all damage modes. As a result, one should strive for obtaining representative and accurate turbine component heat transfer analysis and preparation for component life analysis.

4.4-14 Conclusions

Aircraft propulsion engines, land-based power generation, and industrial machines have, as a primary component, the turbine as means to produce thrust or generate power. In the turbine section of the engine, airfoil components are subjected to extremely complex and damaging environments. The combination of high gas temperatures and pressures, strong gradients, abrupt geometry changes, viscous forces, rotational forces, and unsteady turbine vane/blade interactions, all combine to offer a formidable challenge in terms of turbine durability. Nevertheless, the ultimate goal is to maintain or even improve the highest level of turbine performance and simultaneously reduce the amount of flow needed to achieve this end. Coolant flow is a penalty to the cycle and thermal efficiency, and requires management by characterizing of the turbine airfoil thermal loads and the requirements for film cooling. Despite being a difficult situation to assess, relatively simple correlations can be used to determine the airfoil overall cooling effectiveness in terms of thermal heat load, convective efficiency and film effectiveness. In this context, existing design approaches were presented to characterize airfoil thermal loads and existing airfoil cooling schemes. Emphasis was given to the general characteristics of turbine cooling including film cooling, impingement cooling, and convective cooling for different parts of the airfoil such as leading edge, mid-body, trailing edge, tip and endwalls. Convective cooling is presented in terms of fundamental cooling enhancements. The heat transfer phenomena associated with turbulating trip strips and pedestals were presented and discussed in some detail. In the end, internal and external heat transfer conditions are used to determine the durability of the airfoils in terms of oxidation, creep life and fatigue cycles. Recent literature dealing with these topics is listed to provide more in-depth overview of the subject matter.

4.4-15 Notes

1. J. Moustapha, M.F. Zelesky, N. Baines, and D. Japikse, *Axial and Radial Turbines*, Concepts NREC, 2003
2. Ibid.
3. Ibid.
4. D.P. DeLuca and C.G. Annis Jr, "Fatigue in Single Crystal Nickel Superalloys," Office of Naval research (ONR) FR-23800, Aug. 1995; N.J. Arakere, "High-Temperature Properties of Single Crystal Superalloys in Air and Hydrogen," ASME IGTI 2001-GT-0585, New Orleans, June 2001; R.A. Naik, D.P. DeLuca, and D.M Shah, "Critical Plane Fatigue Modeling and Characterization of Single Crystal Nickel Superalloys," ASME IGTI 2001-GT-30300, *Trans. ASME Journal of Engineering for Gas Turbines and Power*, 2004; D.W. Maclachlan and D.M. Knowles, "The Effect of Material on the Analysis of Single Crystal Turbine Blades: Part I – Material Model," *Fatigue and Fracture Engineering Material Science 25* (2002): 385-398;D.W. Maclachlan and D.M. Knowles, "The Effect of Material on the Analysis of Single Crystal Turbine Blades: Part II – Component Analysis," *Fatigue and Fracture Engineering Material Science 25* (2002): 385-398.
5. V. Seetharaman, "Thickness Debit Properties of PW1484," Pratt and Whitney Materials and Processes Engineering, Interim Report, Nov. 2002.
6. C.T. Sims, N.S. Stoloff, and W.C. Hagel, *Superalloys II*, (John Wiley & Sons, 1980).
7. T.L. Dame, "Anisotropic Constitute Model for Nickel Base Single Crystal Alloys: Development and Finite Element Implementation," PhD Thesis, University of Cincinnati, 1985.
8. F.R.N. Nabarro and H.L. deVillers, *The Physics of Creep*, (Taylor and Francis, 1995).
9. F.J. Cunha, M.T. Dahmer, and M.K. Chyu, "Thermal-Mechanical Life Prediction System for Anisotropic Turbine Components," ASME GT2005-68108, Reno, NV, 2005, Trans. *ASME Journal of Turbomachinery*, 2006.
10. See note 5 above.
11. J.E. Heine, J.R. Warren, and B.A. Cowles, "Thermal Mechanical Fatigue of Coated Blade Materials," Wright-Patterson Final Report ERDC-TR-89-4027, Sept. 1988.
12. See note 1 above.
13. L. Torbidoni and J.H. Horlock, " A New Method to Calculate the Coolant Requirements of a High Temperature Gas Turbine Blade," ASME Paper GT2004-53729, Vienna, Austria, 2004.
14. Ibid.

15. See note 1.
16. H. Schlichting, *Boundary-Layer Theory*, (McGraw-Hill, 7th Edition, 1979).
17. See note 13.
18. Goldstein, R.J., "Film Cooling", Advances in Heat Transfer, Vol. 7, pp. 357-358.
19. See note 1.
20. M.K. Chyu, "Heat Transfer and Pressure Drop for Short Pin-Fin Arrays with Pin-Endwall Fillet." *Trans. ASME Journal of Heat Transfer 112* (1990): 926-932; A.A. Zukauskas, "Heat Transfer from Tubes in Cross Flow," *Advances in Heat Transfer 8* (1972): 116-133.
21. R.J. Goldstein, E.R.G Eckert, and F. Burggraf, "Effects of Hole Geometry and Density on Three-Dimensional Film Cooling," *Trans. ASME J. Heat Transfer*, 1974.
22. J.E. Albert, D.G. Bogard, and F. Cunha, "Adiabatic and Overall Effectiveness for a Film Cooled Blade," IGTI-ASME GT2004-53998, Vienna, Austria, 2004.
23. F.J. Cunha, M. Dahmer, and M.K. Chyu, "Analysis of Airfoil Trailing Edge Heat Transfer and Its Significance in Thermal Mechanical Design and Durability," ASME GT2005-68107, *Trans. ASME Journal of Turbomachinery*, 2006.
24. See note 1.
25. J.K. Salisbury, *Steam Turbines and Their Cycles* (Malabar, FL: R.E. Krieger Publishing Co., 1950).
26. F.J. Cunha, "Integrated Steam/Gas Cooling System for Gas Turbines," US Patent No. 5,340,274, 1994; A. Jacala, R.M. Davis, M.A. Sullivan, R.P. Chyu, and F. Staub, "Closed Circuit Steam Cooled Bucket," US Patent No. 5,536,143, 1996; F.J. Cunha, D.A. DeAngelis, T.A. Brown, S. Chopra, V.H.S. Correia, and D.R. Predmore, "Turbine Stator Vane Segments Having Combined Air and Steam Cooling Circuits," US Patent No. 5,634,766, 1996.
27. L. Langston, "A Year of Turbulence", Power and Energy, *ASME Magazine*, June, 2004.
28. A.H. Lefebre, Gas Turbine Combustion, Taylor and Francis, 2nd Ed., 1999.
29. Ibid.
30. J.C. Han, "Turbine Blade Cooling Studies at Texas A&M University ~ 1980-2004", The 2004 AIAA Thermophysics Award Lecture, 2005.
31. See note 16.
32. Ibid.
33. See note 1.
34. See note 16.
35. See note 1.
36. W.M. Kays and M.E. Crawford, Convective Heat and Mass Transfer, McGraw-Hill, 1980, 2nd Ed.
37. F.O. Soechting and O.P. Sharma, "Design Code Verification of External Heat Transfer Coefficients," Paper No. AIAA-88-3011, 1988.
38. W.M. Kays and M.E. Crawford, "STAN5 - A Program for Numerical Computation of Two-Dimensional Internal and External Flows," NASA CR-27-42, 1976.
39. R.L. McKnight, J.H. Laflen, and Spamer, "Turbine Blade Tip Durability Analysis", NASA CR-165268, Feb. 1981; J. Christophel, K.A. Thole, and F.J. Cunha, "Measured Adiabatic Effectiveness and Heat Transfer for Blowing from Tip of a Turbine Blade," *Trans. ASME Journal of Turbomachinery 127*, (2005): 251-262; J. Christophel, K.A. Thole, and F.J. Cunha, "Cooling the Tip of a Turbine Blade Using Pressure Side Holes – Part I. Adiabatic Effectiveness Measurements," *Trans. ASME Journal of Turbomachinery 127* (2005): 270-277; J. Christophel, K.A. Thole, and F.J. Cunha, "Cooling the Tip of a Turbine Blade Using Pressure Side Holes – Part II: Heat Transfer Measurements," *Trans. ASME Journal of Turbomachinery 127* (2005): 278-286; E. Couch, J. Christophel, E. Hohlfeld, K.A. Thole, and F.J. Cunha, "Comparison of Measurements and Predictions for Blowing from Tip of a Turbine Blade," *AIAA J. of Propulsion and Power 21* (2005): 335-343.
40. M.F. Blair, "An experimental Study of Heat Transfer and Film Cooling on Large-Scale Turbine Endwall," *Trans. ASME J of Heat Transfer 96* (1974): 524-529; R.A. Graziani, M.F. Blair, J.R. Taylor, and R.E. Mayle, "An Experimental Study of Endwall and Airfoil Surface Heat Transfer in a Large Scale Turbine Blade Cascade," *Trans. ASME J. Eng. Gas Turbine Power 102* (1980): 257-267; O.P. Sharma and T.C. Buttler, " Reynolds Stresses and Dissipation Mechanisms Downstream of a Turbine Cascade," *Trans. J of Turbomachinery 109* (1987): 229-236; R.J. Goldstein and R.A. Spores, "Turbulent Transport on the Endwall in the Region Between Adjacent Turbine Blades," *Trans. J of Turbomachinery 110* (1988): 862-869; J.T. Chung and T.W. Simon, "Effectiveness of the Gas Turbine Endwall Fences in Secondary Flow Control at Elevated Freestream Turbulence Levels," ASME Paper 93-GT-51, 1993; Y. Yu and M.K. Chyu, "Influence of Gap Leakage Downstream of the Injection Holes on Film Cooling Performance," *Trans. J of Turbomachinery 120* (1998): 541-548; W.W. Ranson, K.A. Thole, and F.J. Cunha, "Adiabatic Effectiveness Measurements and Predictions of Leakage Flows Along a Blade Endwall, *AIAA J. of Propulsion*, Nov. 2005.
41. F. Kreith, *Principles of Heat Transfer* , IEP- A Dun-Donneley Pub., 1976, 3rd Ed.
42. See note 13.
43. See note 18.
44. See note 21.
45. See note 18.

46. J.C. Han, S. Dutta, and S. Ekkad, *Gas Turbine Heat Transfer and Cooling Technology*, Taylor and Francis, 1st Ed., Ch. 1, 2000.
47. Patankar, S.V., and Spalding, D.B., Heat and Mass Transfer in Boundary Layers, CRC Press, Cleveland, 1968.
48. See note 36.
49. F.M. White, *Viscous Fluid Flow*, McGraw-Hill, 2nd Ed, 1991.
50. See note 41.
51. J. Nikuradse, (1933) " Laws of flow in rough pipes," VDI Forsch.. 361(1933) English Translation. NACA TM-1292 (1965).
52. J.C. Han, "Heat transfer and friction in channels with two opposite rib-roughnened walls," *Trans. ASME Journal of Heat Transfer 106* (1984): 774-781.
53. R.L. Webb, E.R.G. Eckert, and R.J. Goldstein, "Heat transfer and friction in tubes with repeated-rib roughness," *Int. J. Mass Transfer 14* (1971): 601-617; R.L. Webb and E.R.G. Eckert, "Application of rough surfaces to heat exchanger design," *Int. J. Mass Transfer 15* (1972): 1647-1658.
54. Ibid.
55. F.J. Cunha, "Numerical Prediction of Heat Transfer in Internal Cooling Passages of Gas Turbine Blades," *IGTI- ASME Cogen Turbo Power 8* (1993): 307-316; F.J. Cunha, "A Calculation procedure to Analyze Three Dimensional Parabolic Flow Problems of Heat Transfer with Rotation," *ASME HTD 300* (1994): 123-137; D.G.N. Tse and Steuber, "Flow in a Rotating Square Serpentine Coolant Passage with Skewed Trips," ASME Paper 97-GT-529, 1997; J.H. Wagner. B.V. Johnson, R.A. Graziani, and F.C. Yeh, "Heat Transfer in Rotating Serpentine Passages with Trips Normal to the Flow," ASME Paper 91-GT-265, Transactions ASME, 1992.
56. See note 53.
57. U. Uysal, P. Li, M.K. Chyu, and F.J. Cunha, " Heat Transfer on Internal Surfaces of a Duct Subjected to Impingement of a Jet Array with Varying Jet Hole-Size and Spacing," ASME GT2005-68944, *Trans. ASME Journal of Turbomachinery*, 2006; R. Gardon and J. Cohonpue, "Heat Transfer Between a Flat Plate and Jet Air Impinging on It," ASME/AICHE International Heat Transfer Conference Proceedings, 1962; H. Martin, "Heat and Mass Transfer Between Impingement Gas Jets and Solid Surfaces," *Advances in Heat Transfer 13*, 1977.
58. M.K. Chyu, U. Uysal, and P-W Li, "Convective Heat Transfer in a Triple-Cavity Structure Near Turbine Blade Trailing Edge," Proceedings of IMECE'02, International Mechanical Engineers Congress, New Orleans, Nov. 17-22, 2002.
59. See note 46.
60. D.M. Kercher and W. Tabakoff, "Heat Transfer by Square Air Jets Impinging Perpendicular to a Flat Surface Including the Effect of Spent Air," ASME Paper 69-GT-4, *Trans. ASME Journal of Engineering for Power*, 1970; L.M. Florschuetz, C.R. Truman, and D.E. Metzger, " Streamwise Flow and Heat Transfer Distributions for Jet Array Impingement with Crossflow, *Trans. ASME Journal Heat Transfer*, March, 1981.
61. Ibid (Florschuetz).
62. See note 20 (Zukauskas).
63. See note 20 (Chyu).
64. F.W. Dittus and L.M.K. Boelter, *University of California at Berkely Publications in Engineering 2* (1930): 443.
65. K. Ishida and K. Hamabe, "Effect of Pin-Fin Aspect Ratio and Arrangement on Heat Transfer and Pressure Drop of Pin Fin Duct for Airfoil Internal Cooling Passage," ASME Paper 85-WA/HT-62, 1985.
66. See note 46.
67. See note 20 (Chyu).
68. See note 23.
69. Ibid.
70. ANSYS User's Manual, Swanson Analysis Systems, Inc., Volumes I,II,III,IV, Revision 5.0.
71. R.D. Thulin and D.C. Howe, "Energy Efficient Engine High-Pressure Turbine Design Report", NASA CR-165608, PWA-5594-171, March 1982.
72. See note 4 (Maclachlan, 2002).
73. Ibid.
74. F.R. Larson and J. Miller, "A Time-Temperature Relationship for Rupture and Creep Stress," *Transactions of the ASME* (1952): 765-775; F. Garafalo, *Fundamentals of Creep and Creep-Rupture in Metals*, The Macmellan Co.,1965; D.C. Stouffer and L.T. Dame, *Inelastic Deformation of Metals Models, Mechanical Properties and Metallurgy*, John Wiley & Sons, 1st Ed.,1996.
75. D. Burgreen, "Structural Growth Induced by Thermal Cycling," *Journal of Basic Engineering*, ASME 68-WA/Met-14, 1968; F.O. Soechting, "Turbine Low Cycle Fatigue Design Program," Wright-Patterson Final Report AFWAL-TR-86-2124, 1985; also see note 21.

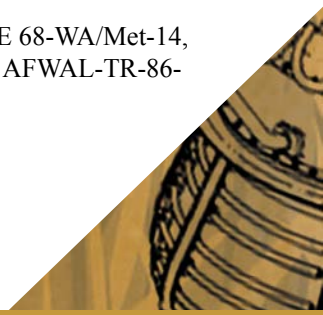

Biography

4.4 Heat Transfer Analysis

Frank J. Cunha, Ph.D., P.E.

Pratt & Whitney
United Technologies Corporation
5 Bruce Lane
Avon, CT 06001

phone: (860) 565-8909
email: frank.cunha@pw.utc.com

Dr. Cunha has worked in the area of turbine cooling design and analysis, heat transfer and mechanical design for a period spanning 25 years. During this time, Dr. Cunha assumed lead design responsibilities at several original equipment manufacturers, including Siemens-Westinghouse, General Electric, and Pratt and Whitney and has received 25 US patents for design of turbine engine hot gas path components. Throughout his career, Dr. Cunha has continued to apply recent advances in cooling technology to both commercial and military engine programs to achieve the highest rotor inlet temperature level in the aerospace industry. Dr. Cunha has been a leader in developing advanced testing cooling programs at a consortium of Universities, and has published numerous journal and symposium technical papers on turbine cooling technologies.